

A Deep Dive into Understanding Tumor Foci Classification using Multiparametric MRI Based on Convolutional Neural Network

Weiwei Zong, Joon Lee, Chang Liu, Eric Carver, Aharon Feldman, Branislava Janic, Mohamed Elshaikh, Milan Pantellic, David Hearshen, Indrin Chetty, Benjamin Movsas, Ning Wen

Henry Ford Health System

{wzong1, JLEE17, CLIU1, ecarver1, afeldma2, bjanic1, MELSHAI1, ICHETTY1, BMOVSA1, nwen1}@hfhs.org {milan, daveh}@rad.hfh.edu

Abstract

Data scarcity has refrained deep learning models from making greater progress in prostate images analysis using multiparametric MRI. In this paper, an efficient convolutional neural network (CNN) was developed to classify lesion malignancy for prostate cancer patients, based on which model interpretation was systematically analyzed to bridge the gap between natural images and MR images, which is the first one of its kind in the literature. The problem of small sample size was addressed and successfully tackled by feeding the intermediate features into a traditional classification algorithm known as weighted extreme learning machine, with imbalanced distribution among output categories taken into consideration. Model trained on public data set was able to generalize to data from an independent institution to make accurate prediction. The generated saliency map was found to overlay well with the lesion and could benefit clinicians for diagnosing purpose.

1. Introduction

Prostate cancer (PCa) is the most common cancer in men in the United States, and it is the second leading cause of cancer death in these patients [1]. Multiparametric magnetic resonance imaging (mpMRI) for PCa has increased in significance over the past decade. mpMRI sequences have shown promise for the

detection and localization of PCa including T2-weighted, diffusion-weighted imaging (DWI), dynamic contrast-enhanced imaging (DCE) and MR spectroscopy. Combining these MR sequences into a multiparametric format has improved the performance characteristics of PCa detection and localization by evaluating area under curve (AUC) values, sensitivities, specificities, and positive predictive values [2, 3]. Prostate biopsy is still considered the golden standard to determine if a suspicious lesion is benign or malignant. However, biopsy is an invasive procedure prone to complications such as hemorrhage, dysuria, and infection. Furthermore, in a small number of cases prostate biopsies can fail to establish the diagnosis despite magnetic resonance- and transrectal ultrasound-guided approaches [4].

Clinically significant cancer is defined on histopathology as Gleason score ≥ 7 (including 3+4) according to PI-RADS™ v2 in order to standardize reporting of mpMRI and correlate with pathology [5]. Also, PCa is a multifocal disease in up to 87% of cases; therefore, the ability to distinguish malignant from benign tissue foci within the prostate is crucial for optimal diagnosis and treatment [6]. This has led to an interest in machine learning and computer vision utilizing mpMRI to non-invasively obtain accurate radiologic diagnoses that correlate their histopathologic variants [7]. Unfortunately, data scarcity is one of the major challenges in applying deep machine learning algorithms in interpreting mpMRI images due to tightly-regulated information acquisition as well as the high cost of MRI acquisition and labeled data from medical experts. In addition, health records cannot be shared without consent due to privacy laws and related healthcare policies and regulations.

Recently, efforts have been made [8, 9] to transfer knowledge from publicly available large-scale data consisting of millions or more natural objects or scene images [10] to medical applications with small scale of data. Unfortunately, limited improvements have been observed compared to training efforts mainly due to the remarkable differences between natural and medical images. In this paper we report a vanilla convolutional neural network (CNN) with an appropriate depth that has been carefully structured to adapt to small data of 201 patients and 320 lesions and to learn from scratch. In addition to classifying lesions into benign or malignant, the purpose of this study was: 1) to provide insight into the cross-modality information of intraprostatic lesions and the entire prostate gland provided by mpMRI sequences; 2) to understand how CNN interprets prostate mpMRI sequences, and 3) to test how a traditional shallow classifier can help improve the accuracy of lesion classification.

2. Cohort

2.1 Data

Data used in the study originated from the SPIE-AAPM-NCI Prostate MR Gleason Grade Group Challenge [11], which aimed to develop quantitative mpMRI biomarkers for determination of malignant lesions in PCa patients. Prostate Ca patients were previously de-identified by SPIE-AAPM-NCI and The Cancer Imaging Archive (TCIA).

The training set consisted of 320 lesion findings from 201 patients and included multiple MR sequences such as T2-weighted (T2W), dynamic contrast-enhanced (DCE) and diffusion-weighted imaging (DWI). T2W images were acquired using a turbo spin echo sequence and had a resolution of around 0.5 mm in-plane and a slice thickness of 3.6 mm. The DWI series were acquired with a single-shot echo planar imaging sequence with a resolution of 2 mm in-plane and 3.6 mm slice thickness and with diffusion-encoding gradients in three directions. Three DWI sequences were acquired (50, 400, and 800 s/mm²) from which the apparent diffusion coefficient (ADC) map was calculated [11].

In the four examples shown in Figure 1, two were malignant lesions while the other two were benign. In the second case (row 2), there was a suspicious lesion in the peripheral zone (PZ) which showed hyperintense signal in both T2W and ADC. Although the k^{trans} was elevated in the prostate, the hyperintensive signal was shown in the central gland (CG) instead. Similarly, the suspicious lesion of the fourth case (row 4) was noticeable in the CG of all four imaging modalities, however, it was classified as the benign lesion based on biopsy results while the third case was considered as malignant.

An independent cohort consisting of 25 patients with 33 lesions was collected for testing from our own institution with IRB-approval. An ultrasound-guided needle biopsy was performed to confirm the diagnosis. Among the 33 lesions, 15 were diagnosed malignant and 18 benign. Two image modalities were acquired from the pelvis of all patients using a 3.0 T MR scanner (Ingenia, Philips Medical System, Best, the Netherlands) using small field of view as follows: T2W acquired with Fast-Spin-Echo (TE/TR: 4389/110ms, Flip Angle: 90° with image resolution of 0.42×0.42×2.4mm³) and DWI with two b values (0 and 1,000 s/mm²). The voxel-wise ADC map was constructed using these two DWIs.

All images were registered to T2-axial image sets and resampled to 1 mm isotropic resolution. Normalization from intensity image to gray image was performed independently for each modality for each patient. Top 1% histogram was clipped for T2W to remove outlier pixels.

2.2 Data Augmentation

Classic augmentation options include rotation, translational shifting, cropping, scaling, adding gaussian or salt-n-pepper noise, etc. We carefully selected rotation and scaling as our augmentation techniques while avoiding adding irrelevant information that might bias the model’s decision-making such as adding noise. A point indicating a lesion’s location was provided in the original dataset for each lesion. With that point as the center, patches of 30x30, 32x32 and 34x34 pixels were cropped. The selection of patch size depended on lesion size for the whole data set and was verified as optimal by experiments. The ratio of malignant versus benign lesions was around 1:3, and this was taken into consideration when performing the image rotation.

3. Methods

3.1 CNN Model and Training

Considering the scale and characteristics of our data, we utilized a vanilla CNN consisting of four convolutional layers, each followed by batch normalization and Relu nonlinear layers, and two max pooling layers after every two convolutional blocks. The number of feature maps for each convolutional layer was 32, 32, 64, and 64, respectively. Fully connected layers consisted of two hidden layers with 512 and 128 hidden nodes, respectively (Figure 2(a)).

The convolutional kernels underwent an orthogonalization process after being randomly initialized, which enforced diversity in learned features (Figure 4). Otherwise, there would be unlearned filters exhibiting blank feature maps. Adam solver was used for optimization. We used 10-fold cross validation in search for optimal meta parameters. The model with optimal parameters was then evaluated on the testing cohort.

3.2 Model Interpretation

Feature maps of intermediate convolutional layers were first visualized. To explore the impact of an individual modality, we trained models on different combinations of modalities and outputted the intermediate feature map visualization for each combination. To compute the ultimate feature map and to explore the discriminant location in the patch we re-trained our model as in class activation map (CAM)

[12]. The re-training process (Figure 2(b)) included representing each feature map of last convolutional layer with a node by global max pooling, removing fully-connected layer while keeping the output nodes and fine-tuning the whole network until converging. The ultimate feature map was computed as a linear combination of the feature maps from the last convolutional layer (Figure 2(c)). The weighting on each feature map was obtained by connecting the weights between the same feature map and the output node from the aforementioned re-trained model. Therefore, the CAM indicates class-related salient locations within the input patch when the model makes predictions.

3.3 CNN Features + Weighted ELM

Extreme learning machine (ELM) was proposed as a simplified substitute for back-propagation (BP) to train a single hidden layer feedforward neural network. In contrast to other popular classification algorithms such as BP-based neural networks or support vector machines (SVMs), solution of ELM was analytically computed instead of iteratively tuned, which makes its implementation outstandingly efficient. A kernelized version of ELM was used in our work. Specifically, a radial basis function (RBF) kernel ($K(\mathbf{u}, \mathbf{v}) = \exp(-\gamma \|\mathbf{u} - \mathbf{v}\|^2)$ with kernel parameter γ to be tuned) was used to transform the data and then parameters of the model were computed as a solution to an optimization problem (Equation 1) that aimed to minimize training errors, as well as the L-2 norm of the parameters to prevent overfitting [13],

$$\text{Minimize: } L_{wELM} = \frac{1}{2} \|\beta\|^2 + C \frac{1}{2} \sum_{i=1}^N w_i \epsilon_i^2 \quad (1)$$

$$\text{Subject to: } h(x_i)\beta = t_i - \epsilon_i, \quad i = 1, \dots, N,$$

where N is the number of samples, β is the weight connecting the hidden and output layers to be analytically computed, $h(x_i)$ is the hidden layer mapping of input x_i , ϵ_i is the error from predicted output ($h(x_i)\beta$) and the targeted output t_i , C is the tunable parameter as a trade-off between training error and L2-norm, and w_i is the weighting assigned to input x_i when computing the loss function. In our experiments, w_i was set inversely proportional to the number of samples class x_i belonged to. Here, kernel is defined as the multiplication of two mapping functions: $K(x_i, x_j) = h(x_i) \cdot h(x_j)$.

4. Results

4.1 Multi-Modality Selection

Cross validation was stratified to evenly extract samples from both categories. Table 1 shows validation results on one of the ten folds with various combinations of modalities as input. When a single MR modality was inputted, functional imaging such as ADC and DWI_{b50} outperformed anatomic imaging (i.e., T2W). Note that by using ADC alone, a slight advantage over using both T2W and ADC was observed. ADC was found better than DWI_{b50} for either single or multiple modality inputs. The best performance of (1, 0.83, 0.91) for (sensitivity, specific, G-mean) was found when a combination of T2W, ADC and DWI_{b50} was inputted. The performance was deteriorated to the level of using ADC alone when k^{trans} was added.

4.2 Lesion Classification

As shown in Table 2, for CNN end-to-end training, the average validation result was (0.53, 0.83, 0.65). Variations among the ten folds were attributed mostly to the heterogeneity of prostate MRI.

We extracted features from intermediate convolutional layers and fully-connected layers and tested and compared their discriminant capability using wELM (Table 3). As shown in Figure 3, no layer consistently outperformed the other layers on every fold. The average G-mean among all ten folds indicated that the features from the third convolutional layer slightly outperformed the other layers. We selected CV7 to demonstrate the substantial performance improvement with the use of wELM as a classifier, as shown in Table 4. (Sensitivity, specificity, G-mean) increased from (0.53, 0.83, 0.65) to (0.76, 0.82, 0.79).

T-sne plots shown in Figure 5 projected data into 2-dimensional space to view the separability among distinct categories. Data points demonstrated a trend in the separation improvement with layer propagation.

Though DWI_{b0} other than DWI_{b50} was used as input for testing set, learned model was found to generalize well to the testing cohort of 33 lesions. 13 out of 15 malignant lesions and 17 out of 18 benign lesions were detected.

4.3 Feature Mapping Visualization

We showed that different imaging sequences had strong impact on classification accuracy. The feature maps learned from each convolutional layer using different combinations of MR sequences as input were discussed and illustrated using the case shown in Figure 4. The best results were achieved using a combination of T2W, DWI_{b50}, and ADC. As shown in Figure 4(a), through visualization of deep feature maps after each convolutional layer, the lower layer was able to capture the edges of each structure including the prostate, rectum and obturator internus muscles, and the sub-regions inside the prostate including the CG and PZ. The feature map also covered a spectrum of intensity changes contributed from each image modality. As it moved to the deep layers, the spatial resolution of the feature maps was reduced and focused on the abnormal regions where the lesion resided, and the learned features tended to be more abstract and task related. As shown in the feature maps of the last layer, the lesion (blue) was visible in a majority of the feature maps and a hypointense area (red) in the lesion's close proximity was also included in a subset of feature maps. These feature maps were passed to the fully connected layer and used for classification. This observation was consistent with that on natural color images [14].

The combination of T2W, DWI, and DCE has been shown to provide high sensitivity and specificity in intraprostatic lesion identification and has been recommended for lesion detection in current consensus guidelines [15]. We also investigated why our model performance was degraded by adding k^{trans} . As shown in Figure 4(b), the k^{trans} map was added as an additional input. There were two regions elevated in the k^{trans} map, a brighter area in the CG and a relatively less intense area in the lesion. By incorporating this information in the learning, the model was able to capture additional information from the k^{trans} of the first layer. However, we observed that the feature maps shifted toward the CG which was shown in the last layer. The lesion was observable in most of the feature maps. It clearly induced more uncertainty in the classification task and reduced model performance.

DWI has been shown to have good sensitivity and specificity for identification of PCa. We repeated a similar procedure to learn how the features were learned using ADC and DWI_{b50} alone (Figure 4(c)). Considering that DWI measures water molecules' diffusion behavior, it lacks anatomical and structural information important for identifying the edges and location of each structure. Hence, in the first layer, a portion of feature maps missed detailed information and were hardly visible. These feature maps were propagated to deeper layers and created very noisy maps. The lesion (hypointense on ADC and hyperintense on DWI_{b50}) was captured in a majority of feature maps in the last layer. It was difficult to make classifications based on these feature maps considering reduced features of the shape, location etc.

We investigated the model performance on lesion classification based on different combinations of MR sequences as input. By investigating the feature maps at each layer, it gained better understanding of how the CNN model was trained, and this information can significantly contribute developing a better strategy for lesion classification using MR images. Clearly, T2W provides morphological features important in identifying lesion shapes and locations. Considering the high sensitivity and specificity values, DWI and ADC are critical imaging modalities in PCa detection. DWI plus T2W was significantly more sensitive and accurate than T2W alone in tumor volume measurement accuracy [16]. Kim et al. [17] showed that the combination of T2W and DWI improved the area under receiver operating characteristics curve (AUC) from 0.61 to 0.88 under clinical interpretation. The addition of DWI to T2W improved PCa localization performance, with AUC increased from 0.66 to 0.79 in the prospective studies [18]. Here, we achieved excellent classification accuracy using the combination of T2W and DWI. Though k^{trans} has been shown to improve the lesion detection in the clinical setting, caution need to be taken when integrating k^{trans} into training. As discussed earlier, the elevated k^{trans} values were present in both lesions and other areas with similar microvascular conditions such as benign prostatic hyperplasia, or vascular enlargement in the gland. It induced higher false positive rates in the model. A potential solution is to split the data into CG and PZ and to train the model separately based on the anatomical structures. This strategy needs further investigation.

4.4 Saliency Map

CAM provides important clues on where the model is looking when making a decision. Figure 6 (a) displayed CAM calculated based on 34x34 pixel patches of two easy cases in PZ, two easy cases in CG and one difficult case with low contrast in T2W. Lesions in PZ were all highlighted exclusively. For lesions in CG, one disconnected region was highlighted in addition to the lesion, which was also considered highly suspicious. The detected region-of-interest (ROI) was found to overlay well with lesions from the original T2W input.

We then tested on 64x64 pixel patches to see if filters learned from small patch size can generalize to cases with a bigger patch size. As can be seen from Figure 6 (b), the learned CNN model was able to detect lesions exclusively within the prostate and exclude adjacent organs such as the bladder and rectum. For the first two cases, the prostate boundary (white circled) was also highlighted. The fifth and sixth cases showed patients with two lesions in the PZ zone, circled in blue and red, respectively. In the fifth case,

both lesions were successfully detected and located; while in the sixth case, the lesion circled in red failed to be detected, mainly because it was cut off in the input images.

This indicated potential application of using CAM for intraprostatic lesion delineation for diagnostic and therapeutic purposes.

4.5 Network Depth and Discussions

There has been a debate about whether deeper layers are necessary in the field of computer vision. In general, it is mostly dependent on the data size and problem complexity. In our case of prostate MRI study, the lower layers can detect low-level features such as boundaries and contrast changes; deeper layers were able to detect semantic features such as lesions which were based on the features extracted at lower layers. By examining the discriminating power of features learned at each layer, a third convolutional layer often provided the best result.

5. Discussions and Related Work

A popular branch of prostate MRI analysis used hand crafted radiomics features [11, 19] which typically requires accurate lesion delineation to extract features that differentiate lesions and normal tissues. Therefore, we will focus on comparing with deep learning models, which can learn data from scratch.

Very few works in the literature have used deep learning models to analyze prostate MRI mainly because of data heterogeneity and small sample size. One work [6] has inspired our work with similar CNN model and trained on the same data. They selected 87% samples to train while we did 10-fold cross validation. Besides image rotation, they augmented data by random shearing and translation based on cropped 32x32 pixel patches. We used multi-scale patches sized 30x30, 32x32 and 34x34. They achieved (0.92, 0.89, 0.89) for (AUC, sensitivity, specificity) on validation data while ours were (0.92, 1.00, 0.83). By extracting learned features and feeding into traditional classifier (sensitivity, specificity) was elevated further to (1.00, 0.92).

Another contribution of this work is model visualization. For the best of our knowledge, no work in the literature has visualized medical images through deep learning models. We visualized learned features in CNN, plotted data separability for each layer, and calculated saliency map to find out what network has learned and focused on layer after layer. Quantitative evaluation of binary classification can be biased. A

random guess can reach 50% accuracy. Only through visualization, we found out that attention was paid to lesion and its surrounding tissues, that assured our confidence in the developed CNN model and what it has learned.

Note that, we used cropped patches, with sizes of 30x30 to 34x34. Such selection was based on the lesion size in the training data and may face challenges in generalizing to patients with lesion sizes out of that range. Performance of the model would deteriorate when the patch size is too large and contain multiple foci. This could be considered a challenge to be tackled in future work to identify the malignancy of multiple foci within the same image patch.

Table 1. Validation results on one-fold of data with different combinations of modalities as input. It can be observed that T2W + ADC + DWI_{b50} is optimal.

CV7 modality combinations	T2W	ADC	DWI _{b50}	T2W +ADC	T2W +DWI _{b50}	ADC + DWI _{b50}	T2W +ADC + DWI _{b50}	T2W +ADC + DWI _{b50} + k ^{trans}
Sensitivity	0.57	0.71	0.71	0.71	0.43	0.86	1.00	0.71
Specificity	0.63	0.88	0.83	0.79	0.88	0.88	0.83	0.88
G-mean	0.60	0.79	0.77	0.75	0.62	0.87	0.91	0.79

Table 2. 10-fold cross validation (CV) results using convolutional neural network end-to-end training. For each fold, there are about 7 malignant and 24 benign lesions. Sensitivity of 0.29 is the same as 2 out of 7 malignant lesions being detected. G-mean is the square root of product of sensitivity and specificity as a metric commonly used for imbalanced data.

	CV1	CV2	CV3	CV4	CV5	CV6	CV7	CV8	CV9	CV10
Sensitivity	0.67	0.43	0.71	0.29	0.43	0.57	1.00	0.43	0.29	0.46
Specificity	0.88	0.92	0.88	0.79	0.83	0.83	0.83	0.79	0.75	0.82
G-mean	0.77	0.63	0.79	0.48	0.60	0.69	0.91	0.58	0.47	0.61
AUC (patch)	0.71	0.73	0.89	0.54	0.64	0.76	0.92	0.67	0.49	0.69
Accuracy (patch)	0.81	0.80	0.85	0.67	0.68	0.78	0.85	0.71	0.64	0.72

Table 3. 10-fold cross validation (CV) results using features from the third convolutional layer and weighted extreme learning machine as the classifier. Compared to CNN end-to-end training, average performance increased from (0.53, 0.83, 0.65) to (0.76, 0.82, 0.79) for (sensitivity, specific, G-mean). C for convolutional layer and FC for fully-connected layer.

	CV1	CV2	CV3	CV4	CV5	CV6	CV7	CV8	CV9	CV10
Sensitivity	1.00	0.71	1.00	0.57	0.71	0.57	1.00	0.71	0.71	0.62
Specificity	0.84	0.83	0.83	0.67	0.92	0.92	0.92	0.75	0.79	0.75

G-mean	0.92	0.77	0.91	0.62	0.81	0.72	0.96	0.73	0.75	0.68
--------	------	------	------	------	------	------	------	------	------	------

Table 4. Validation results for best performing cross validation fold CV7 when features from different CNN layers were used as input for weighted extreme learning machine (wELM). By using wELM, performance increased from (1, 0.83, 0.91) to (1, 0.92, 0.96), the same as two more benign lesions being correctly classified. C for convolutional layer and FC for fully-connected layer.

CV7 CNN features+ wELM	C1	C2	C3	C4	FC1	FC2
Sensitivity	1.00	1.00	1.00	1.00	0.86	1.00
Specificity	0.88	0.79	0.92	0.83	0.88	0.83
G-mean	0.94	0.89	0.96	0.91	0.87	0.91

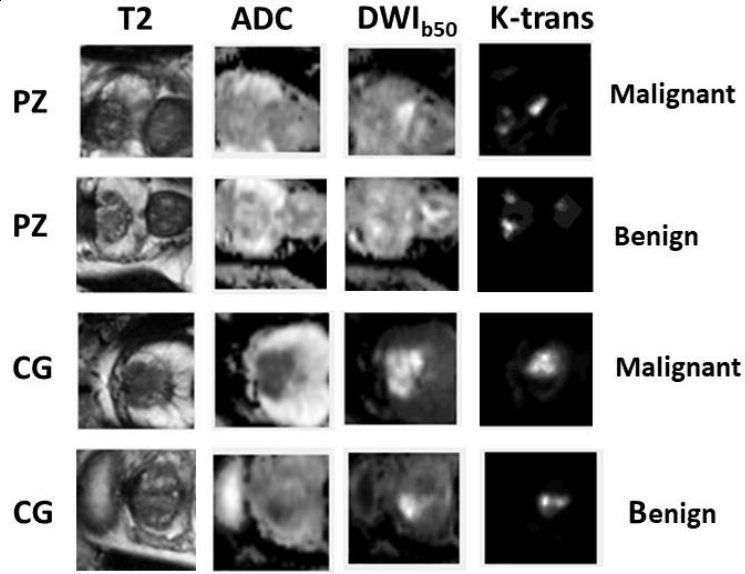
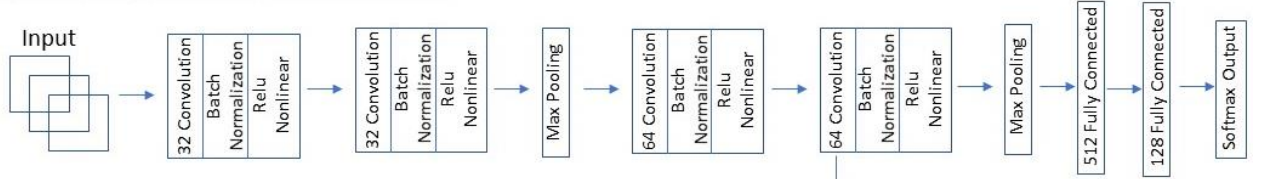
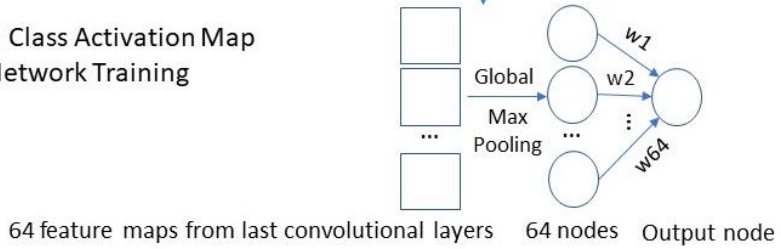


Figure 1. Display of T2, ADC, DWI_{b50} and k^{trans} of 2 malignant and 2 benign 64 x 64 patches including lesions residing in the PZ and CG, respectively. Pitfalls of each sequence can be observed as further illustrated in the text.

(a) Convolutional Neural Network Structure



(b) Class Activation Map
- Network Training



(c) Class Activation Map
- Map Calculation



Figure 2. (a) Illustration of the Convolutional neural network (CNN) structure. (b) To calculate the class activation map (CAM), pre-trained CNN was truncated until the last convolutional layer and concatenated with a global pooling layer and output node. This new network was then fine-tuned based on parameters trained at stage (a). (c) The CAM was calculated as linear combination of feature maps from the last convolutional layer. Weighting on each feature map was learned from stage (b).

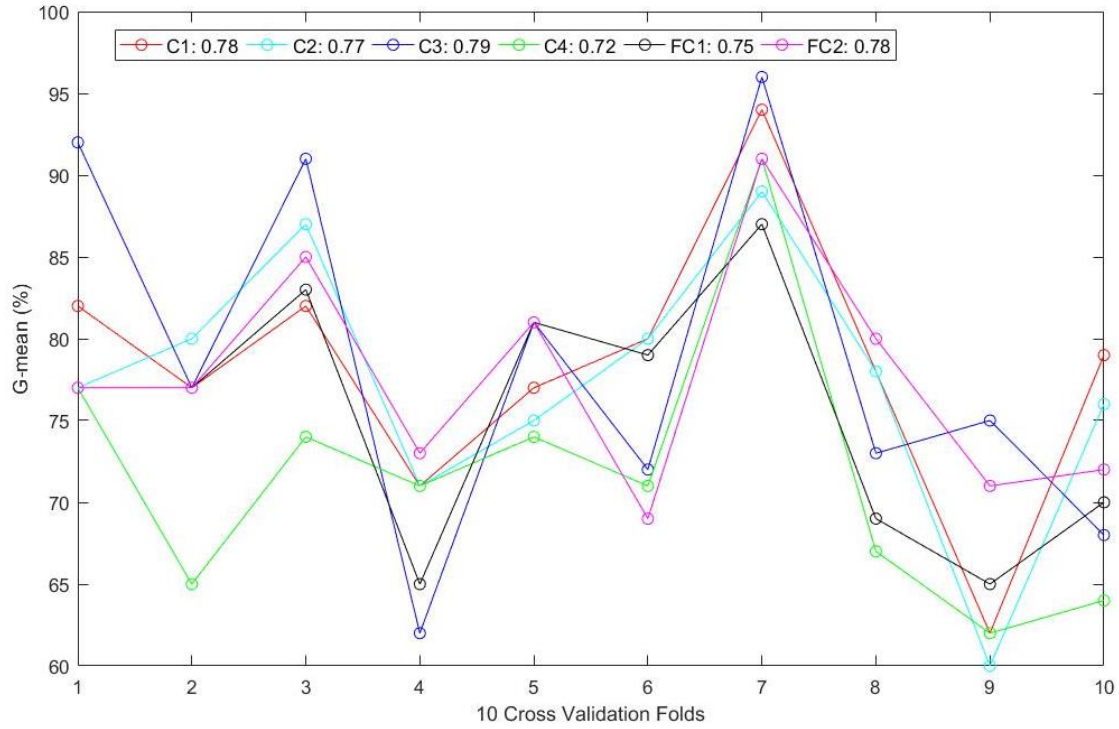
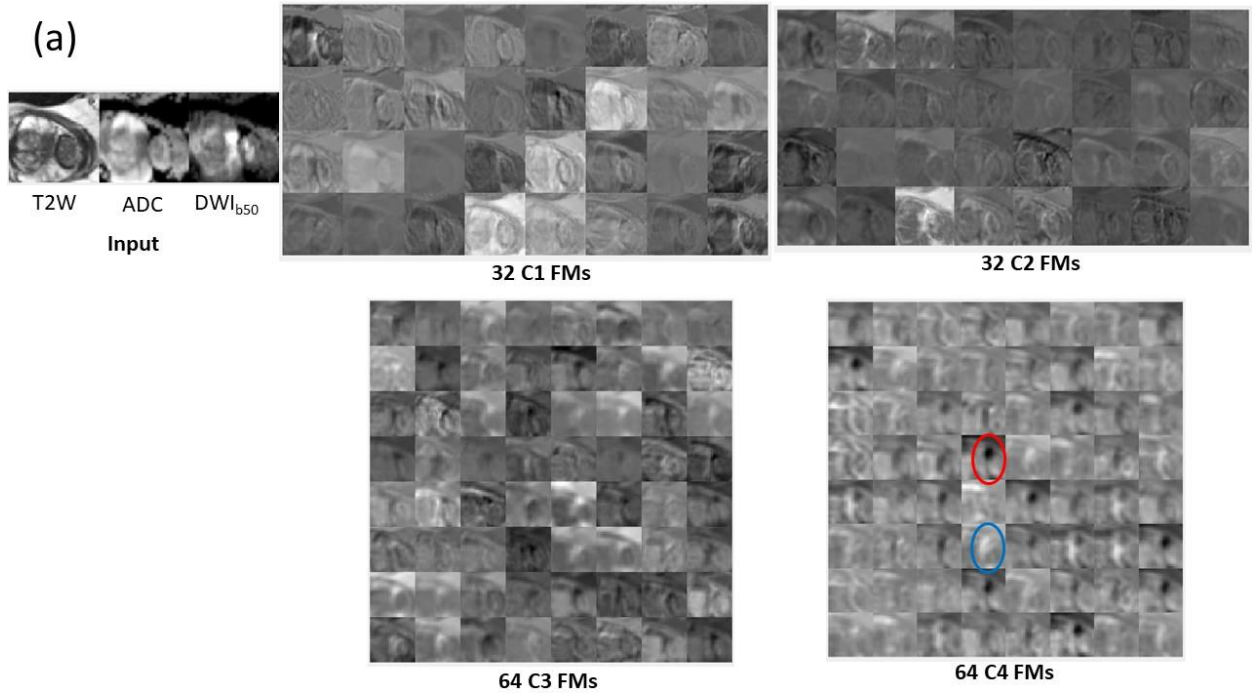


Figure 3. Validation results in terms of G-mean when features were extracted from different layers of CNN. 'C1: 0.78' represents the plot generated with features from C1 and the average result among all ten folds of 0.78. Abbreviation: Convolutional Layer – C; Fully connected layer – FC.



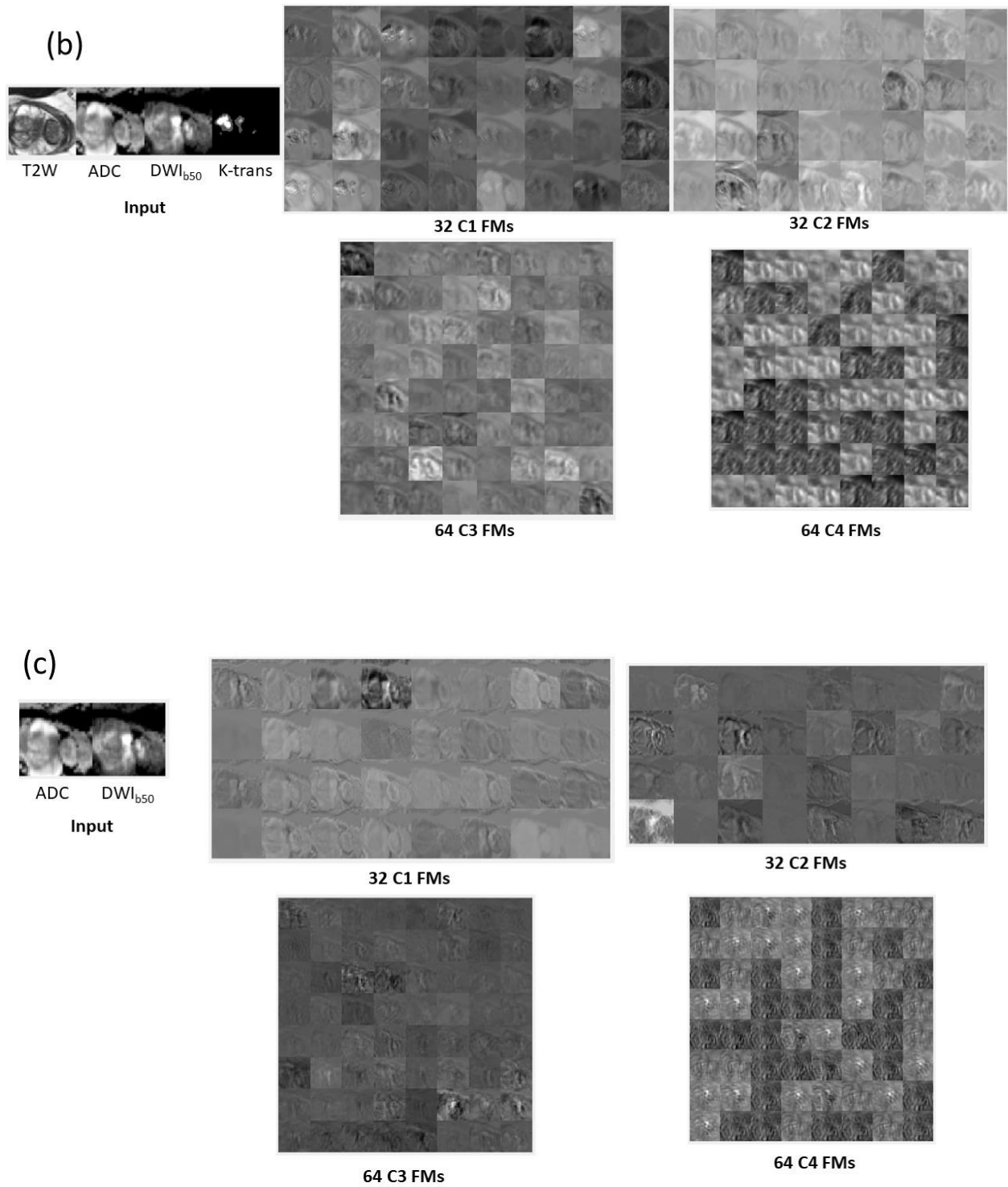


Figure 4. Visualization of intermediate feature mappings for every convolutional layer with respect to a malignant lesion in PZ. (a) Model trained with T2, ADC and DWI_{b50} as multi-channel input successfully

detected the lesion as malignant; (b) model with T2, ADC, DWI_{b50} and k^{trans} as input; (c) and model with ADC and DWI_{b50} as input both failed. Moreover, (a) exhibits rich and hierarchical features. C1 stands for convolution layer 1, similarly for C2, C3, C4 as well. FMs is short for feature mappings.

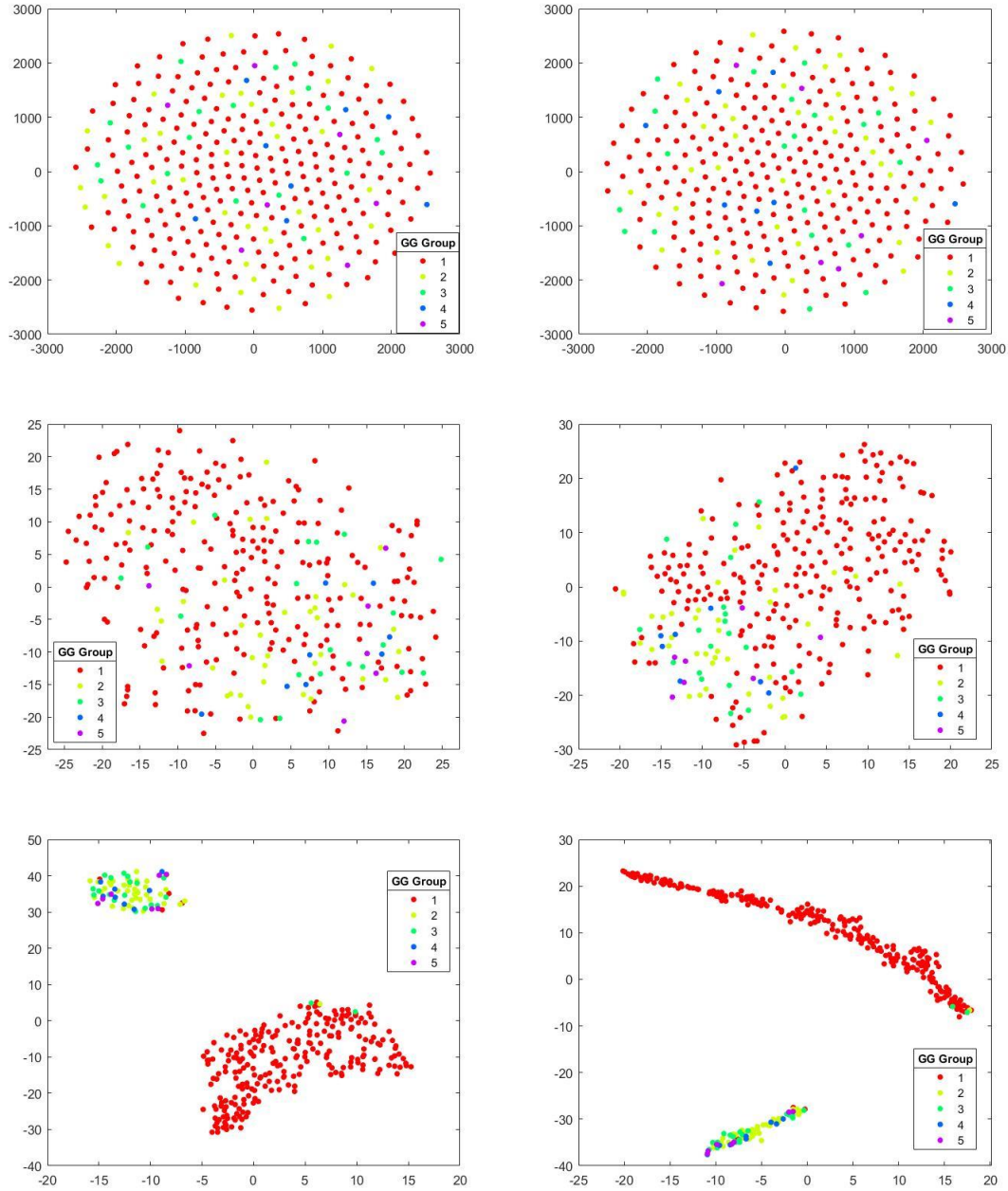
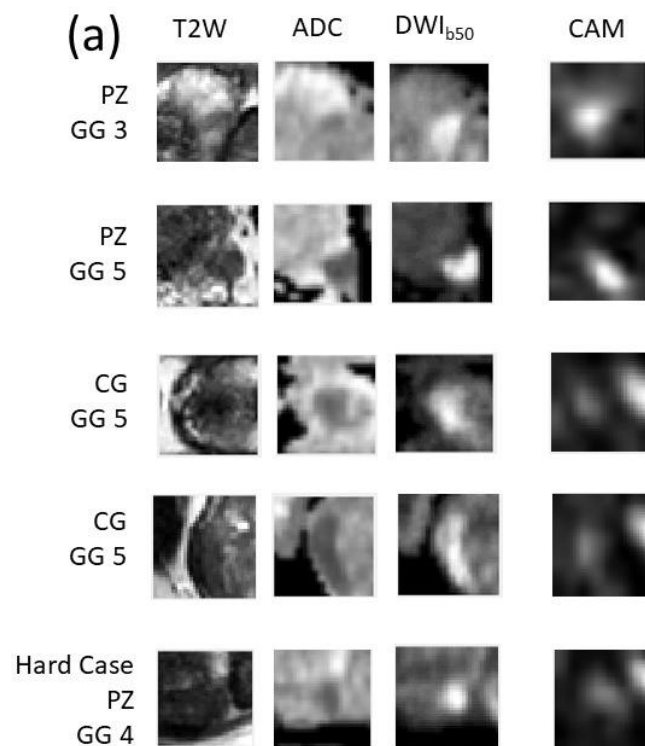


Figure 5. T-sne plots of lesions from CV7 represented by features from different layers. As layer propagated, data became more separable. Gleason Grouping Group 1 was defined as benign and 2 and above as malignant in this study.



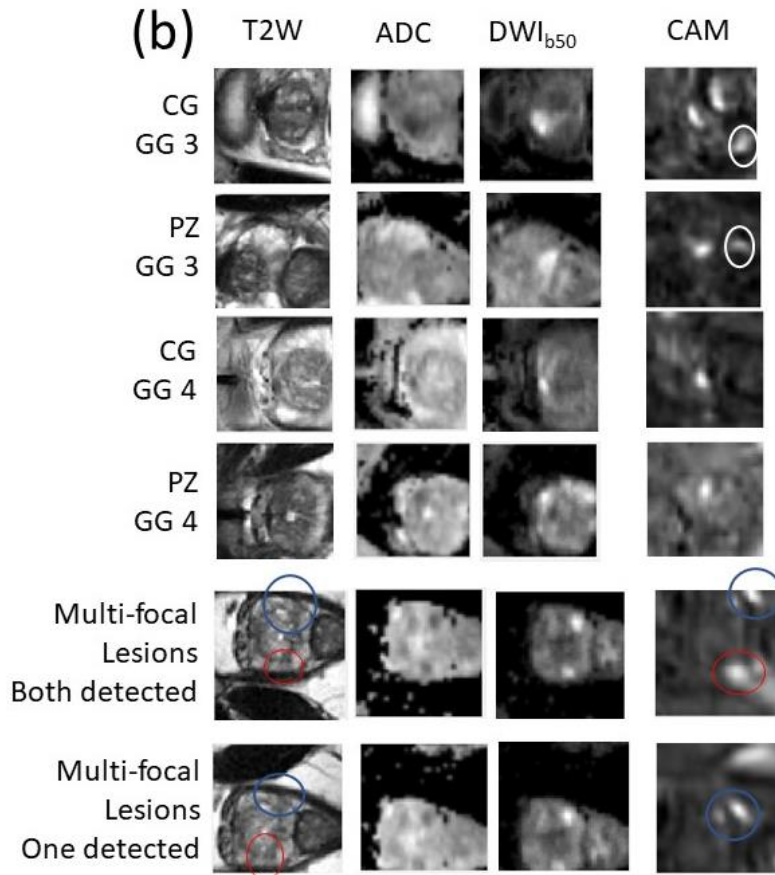


Figure 6. (a) Class activation map (CAM) of cases with 34x34 pixel patch input. (b) Filters learned from 34x34 pixel patch can generalize well to 64x64 pixel patch, where all lesions were exclusively detected in most cases. The computed saliency maps were found overlay well with lesions on original input, thus having potential for real clinical applications. Abbreviations: GG – Gleason grade Group; PZ – peripheral zone; CG – central gland.

Reference

1. <https://www.cancer.org/cancer/prostate-cancer/about/key-statistics.html>. American Cancer Society.
2. Delongchamps, N. B., Rouanne, M., Flam, T., Beuvon, F., Liberatore, M., Zerbib, M., & Cornud, F. (2011). Multiparametric magnetic resonance imaging for the detection and localization of prostate cancer: combination of T2-weighted, dynamic contrast-enhanced and diffusion-weighted imaging. *BJU international*, 107(9), 1411-1418.

3. Dickinson, L., Ahmed, H. U., Allen, C., Barentsz, J. O., Carey, B., Futterer, J. J., ... & Persad, R. (2011). Magnetic resonance imaging for the detection, localisation, and characterisation of prostate cancer: recommendations from a European consensus meeting. *European urology*, 59(4), 477-494.
4. Schouten, M. G., van der Leest, M., Pokorny, M., Hoogenboom, M., Barentsz, J. O., Thompson, L. C., & Fütterer, J. J. (2017). Why and where do we miss significant prostate cancer with multiparametric magnetic resonance imaging followed by magnetic resonance-guided and transrectal ultrasound-guided biopsy in biopsy-naïve men?. *European urology*, 71(6), 896-903.
5. Weinreb, J. C., Barentsz, J. O., Choyke, P. L., Cornud, F., Haider, M. A., Macura, K. J., ... & Thoeny, H. C. (2016). PI-RADS prostate imaging-reporting and data system: 2015, version 2. *European urology*, 69(1), 16-40.
6. Liu, S., Zheng, H., Feng, Y., & Li, W. (2017, March). Prostate cancer diagnosis using deep learning with 3D multiparametric MRI. In *Medical Imaging 2017: Computer-Aided Diagnosis* (Vol. 10134, p. 1013428). International Society for Optics and Photonics.
7. Meiers, I., Waters, D. J., & Bostwick, D. G. (2007). Preoperative prediction of multifocal prostate cancer and application of focal therapy: review 2007. *Urology*, 70(6), S3-S8.
8. Tajbakhsh, N., Shin, J. Y., Gurudu, S. R., Hurst, R. T., Kendall, C. B., Gotway, M. B., & Liang, J. (2016). Convolutional neural networks for medical image analysis: Full training or fine tuning?. *IEEE transactions on medical imaging*, 35(5), 1299-1312.
9. Litjens, G., Kooi, T., Bejnordi, B. E., Setio, A. A. A., Ciompi, F., Ghafoorian, M., ... & Sánchez, C. I. (2017). A survey on deep learning in medical image analysis. *Medical image analysis*, 42, 60-88.
10. Deng, J., Dong, W., Socher, R., Li, L. J., Li, K., & Fei-Fei, L. (2009). Imagenet: A large-scale hierarchical image database.
11. Litjens, G., Debats, O., Barentsz, J., Karssemeijer, N., & Huisman, H. (2014). Computer-aided detection of prostate cancer in MRI. *IEEE transactions on medical imaging*, 33(5), 1083-1092.
12. Zhou, B., Khosla, A., Lapedriza, A., Oliva, A., & Torralba, A. (2016). Learning deep features for discriminative localization. In *Proceedings of the IEEE conference on computer vision and pattern recognition* (pp. 2921-2929).
13. Zong, W., Huang, G. B., & Chen, Y. (2013). Weighted extreme learning machine for imbalance learning. *Neurocomputing*, 101, 229-242.
14. Zeiler, M. D., & Fergus, R. (2014, September). Visualizing and understanding convolutional networks. In *European conference on computer vision* (pp. 818-833). Springer, Cham.
15. Barentsz, J. O., Richenberg, J., Clements, R., Choyke, P., Verma, S., Villeirs, G., ... & Fütterer, J. J. (2012). ESUR prostate MR guidelines 2012. *European radiology*, 22(4), 746-757.
16. Vargas, H. A., Akin, O., Franiel, T., Mazaheri, Y., Zheng, J., Moskowitz, C., ... & Hricak, H. (2011). Diffusion-weighted endorectal MR imaging at 3 T for prostate cancer: tumor detection and assessment of aggressiveness. *Radiology*, 259(3), 775-784.

17. Kim, C. K., Park, B. K., Lee, H. M., & Kwon, G. Y. (2007). Value of diffusion-weighted imaging for the prediction of prostate cancer location at 3T using a phased-array coil: preliminary results. *Investigative radiology*, 42(12), 842-847.
18. Lim, H. K., Kim, J. K., Kim, K. A., & Cho, K. S. (2009). Prostate cancer: apparent diffusion coefficient map with T2-weighted images for detection—a multireader study. *Radiology*, 250(1), 145-151.
19. Chaddad, A., Kucharczyk, M., & Niazi, T. (2018). Multimodal radiomic features for the predicting gleason score of prostate cancer. *Cancers*, 10(8), 249.